Supplementary Information

Engineering Buried Interface by A Conductive Polymer to Mediate Carrier Behavior for Efficient Solar-driven Water Splitting on Si-based Photocathode

Ying Qiang,[1,2] Xiying Fu,[3] Yongjian Jia[1,2]

1. National Engineering Research Center for Technology and Equipment of Environmental Deposition, Lanzhou Jiaotong University, Lanzhou 730070, China;
2. Key Lab of Opt-Electronic Technology and Intelligent Control of Ministry of Education, Lanzhou Jiaotong University, Lanzhou 730070, China;
3. College of Material Science and Engineering, Hebei University of Engineering, Handan 056038, China

Corresponding author's email: Jiayj88@hotmail.com

Supplementary Note S1:

Chemicals and materials

Single-crystalline *p*-Si (100) wafers (one-side polished) with a starting thickness of 625±25 μm, diameter of 6 inches and resistivity of 0.1-1 Ω cm were obtained from Kaihua Crystal Chip Electronics Co., Ltd. Potassium hydroxide purchased (KOH, ≥ 98%), hydrogen peroxide (H_2O_2,30%), ammonia (NH_4OH,) and sodium chloride (NaCl, 99.5%) were purchased from China National Pharmaceutical Group Chemical Reagent Co., Ltd. Potassium hexacyanoferrate(III) ($K_3[Fe(CN)_6]$≥99%) and Tetra-n-Butylammonium hexafluorophosphate (n-Bu_4NPF_6, 99%) was purchased from Anhui Zesheng Technology Co., Ltd. Silver nitrate ($AgNO_3$, 99.8 %) and hydrochloric acid (HCl) were provided by Nanjing Chemical Reagent Co., Ltd. Triethanolamine ($C_6H_{15}NO_3$, 99%) was supplied by Shanghai Sa'en Chemical Technology Co., Ltd. Cadmium acetate dihydrate ($C_4H_6CdO_4$, 99.5%) was supplied by Shanghai Zhongqin Chemical Reagent Co., Ltd.

Sodium thiosulfate pentahydrate ($Na_4S_2O_3·5H_2O$, 99.5%) was purchased from Yantai Shuangshuang Chemical Co., Ltd. Cobalt (II) chloride hexahydrate ($CoCl_2·6H_2O$, 99%) and Boric acid (H_3BO_3, 99%) were provided by Sichuan Xilong Scientific Co., Ltd. Sodium dihydrogen phosphate anhydrous (NaH_2PO_4, 99%) was supplied by Anhui Senrise Technology Co., Ltd. Dichloromethane (CH_2Cl_2, 99%), 3-Chlorothiophene (C_4H_3ClS, 98%) and Pyrrole (C_4H_5N, 99%) were obtained from Lianlong Bohua (Tianjin) Pharmaceutical Chemistry Co., Ltd. Aniline (C_6H_7N, 99.5%) was purchased from Shanghai Maclean's Biochemical Technology Co., Ltd. 2,3-Dihydrothieno[3,4-b]-

1,4-dioxin ($C_6H_6O_2S$, 99%) and Thiophene (C_4H_4S, 99%) were provided by Shanghai Titan Scientific Chemistry Co., Lt. Acetonitrile (CH_3CN,≥99%) was produced by Chengdu Kelong Chemical Co., Ltd. N_2 gas (99.999%) was obtained from Lanzhou Yulong Gas Co., Ltd.

All chemicals were used as received without further purification.

Characterizations

The obtained samples were characterized by X-ray powder diffraction (XRD) on a Bruker D8 ADVANCE X-ray diffractometer using Cu Kα radiation (operating voltage: 40 kV, operating current: 200 mA, scan rate: 5° min^{-1}). The morphologies of the electrodes were performed by a Quanta 200 FEG scanning electron microscope (SEM) equipped with an energy dispersive spectrometer (accelerating voltage of 20 kV). X-ray photoelectron spectroscopy (XPS) measurements were performed by Thermo SCIENTIFIC Nexsa with monochromatized Al Kα excitation (hv=1486.6eV). The binding energy was calibrated using the C 1s photoelectron peak at 284.8 eV as the reference. The thickness of the materials was measured by probe profilometer (Dektak XTL, Bruker). The steady-state photoluminescence (PL) measurements were carried out on a photoluminescence spectrometer using a xenon arc lamp (F-7100, Hitachi, Japan, excitation of 400 nm)

Supplementary Note S2:

Fabrication of Photocathode

1. Wet chemical etching of Si pyramid

Solar-grade *p*-type crystalline Si (100) wafers were cut into pieces and cleaned with a standard RCA process to remove all contaminants on the pristine Si substrate. In a typical process, at the very first step, this silicon substrate is cleaned by RCA1 solution ($NH_4OH:H_2O_2:H_2O$=1:1:5) then in RCA2 solution ($HCl:H_2O_2:H_2O$=1:1:6) for 10 minutes at 70^oC in each case. After that, the clean Si wafers were soaked in a 50 mL etchant solution containing 2 wt% KOH and 2.5 mL isopropanol at 80 °C for 30 min for SiP formation.

2. Assembly of Si-based photocathodes

A Ga/In eutectic alloy was coated on the back of a Si wafer and attached to a copper bar. Conductive silver paint was then applied to affix the copper bar. After drying edges, some parts of the front surface and the whole back surface of the Si wafer were sealed with non-conductive epoxy to expose an active area of ~0.36 cm^2.

3. The Polymer loading on p-Si wafers

Si/PTH: 1.5 mM thiophene was added in a mixed solvent of CH_3CN and CH_2Cl_2 (volume ratio 3:1) consisted with 0.1 M n-Bu_4NPF_6 as the electrolyte. A Pt counter electrode and an Ag/Ag^+ reference electrode were employed. Electrodeposition was conducted at a potential of 2.5 V vs. Ag/Ag^+ for a contain time. After that, the obtained SiP electrode was then dried with a nitrogen gun.

Si/PPy: The work electrode was immersed in an acetonitrile/ dichloromethane (3:1)

solution

containing pyrrole (3 mM). The electropolymerization was conducted in a three-electrode system at room temperature for 60 min at a constantly applied voltage of 0.95 V vs Ag/AgCl. Subsequently, the PPy film was rinsed by acetonitrile and ethanol several times and then dried under argon.

Si/PEDOT:0.01 M 3,4-Ethylenedioxythiophene was added inCH_3CN consisted with 0.01 M $LiClO_4$. A Pt counter electrode and an Ag/Ag^+ reference electrode were employed. Electrodeposition was conducted at a potential of 1.2 V vs. Ag/Ag^+ for a contain time. After that, the obtained Si electrode was then dried with a nitrogen gun.

Si/3-Cl PTH: 0.02 mM 3-Chlorothiophene was added inCH_3CN consisted with 0.1 M n-Bu_4NPF_6 as the electrolyte. A Pt counter electrode and an Ag/Ag^+ reference electrode were employed. Electrodeposition was conducted at a potential of 1.8 V vs. Ag/Ag^+ for a contain time. After that, the obtained Si electrode was then dried with a nitrogen gun.

Si/PANI: Within a CV method, a PANI thin film was deposited on recleaned SiP wafers ranged from -1.2 V to 0.2 V vs. Ag/AgCl for a contain time, using a precursor solution of 0.5 M aniline and 0.5 M H_2SO_4. Subsequently, each PANI-covered SiP wafer was then dried with a nitrogen gun.

4. Deposition of CdS films

The solution of 0.2 M $(CH_3COO)_2Cd{\cdot}2H_2O$ and 0.2 M $Na_4S_2O_3{\cdot}5H_2O$ was adjusted pH to approximately 2.7 to use as the electrolyte. The electrodeposition process was carried out at a three-electrode configuration with the Si electrode as the working

electrode (WE), saturated Ag/AgCl electrode (3 M KCl) as the reference electrode (RE), and carbon rod as the counter electrode (CE). A constant current electrodeposition was carried out at 1.4 V under 75 °C for a certain time. Then, the obtained electrode was taken out and washed by deionized water and ethanol successively.

5. Light-assisted electrodeposition of Co-P

The Co-P was deposited using an electrodeposition process. boric acid (H_3BO_3, 0.15 M), sodium chloride (NaCl, 0.1 M), Cobalt(II) chloride hexahydrate ($CoCl_2 \cdot 6H_2O$, 0.2 M), and sodium phosphite (NaH_2PO_3, 0.06 M) were added in 50 mL water as the electrolyte. A Pt counter electrode and an Ag/AgCl reference electrode were employed. Electrodeposition was carried out at a potential of -0.75 V vs. Ag/AgCl for a certain time. Before starting the deposition, the light source was turned on. After the deposition current stabilized, the light source was shielded to carry out the electrodeposition.

6. Fabrication of Photoanode

Fabrication of TiO_2 nanotube arrays

TiO_2 nanotube arrays were prepared using a two-step anodization process in an electrolyte consisting of ethylene glycol with 0.3 wt.% NH_4F and 2 wt.% H_2O. Titanium foils (99.4% purity, 0.1 mm thickness) were used. The process began with ultrasonic cleaning of the titanium foils in chloroform, acetone, and ethanol for 10 minutes each, followed by drying. The first anodization was carried out at 60 V for 1 hour, using the titanium foil as the anode and a graphite plate as the cathode. After a uniform oxide

layer formed, the samples were cleaned in a 1:1 ethanol-deionized water solution to remove the oxide. The second anodization, also at 60 V but for 2 hours, was conducted while maintaining the electrolyte at 5 ℃ to ensure uniform growth of titanium dioxide nanotubes. Post-anodization, the samples were immersed sequentially in ethylene glycol, a 1:1 mixture of ethylene glycol and acetone, and pure acetone, each for 30 minutes, followed by rinsing and drying. Finally, the samples were annealed in a muffle furnace at 450°C for 1 hour, with a 1 hour ramp-up time, and then cooled naturally.

Deposition of CdS films on Ti/TiO_2

An electrolyte solution containing 0.2 M $Cd(CH_3COO)_2 \cdot 2H_2O$ and 0.2 M $Na_2S_2O_3$ was used, after its pH was adjusted to about 2.7 with concentrated H_2SO_4. The electrodeposition process was carried out at a three-electrode configuration with the Si electrode as the working electrode (WE), saturated Ag/AgCl electrode (3 M KCl) as the reference electrode (RE), and carbon rod as the counter electrode (CE). A constant current electrodeposition was carried out at 1.4 V under 75 °C for 20 minutes. Then, the obtained electrode was taken out and washed by deionized water and ethanol successively.

Fabrication of Ti/TiO_2/CdS/ZnSe photoanode

Hydrothermal route was utilized for the preparation of ZnSe nanoparticles. 0.05 M selenium powder, 0.1 M zinc nitrate and 4.0 M KOH were mixed to form a mixture solution. After thoroughly stirring until evenly mixed, a reducing agent of 1.3 M $HONH_3Cl$ was slowly dripped, which is conducive to the formation of ZnSe nanoparticles. Before adding the mixed solution, place the titanium sheet with the CdS

thin film into the autoclave. Finally, carry out heat treatment at 180°C for 3 hours. Once mixture has been cooled to ambient temperature, it was extracted from the autoclave and subjected to three consecutive washes with water and ethanol, as Photoanode $Ti/TiO_2/CdS/ZnSe$.

Supplementary Note S3:

Photoelectrochemical measurements

A three-electrode measurement configuration was employed using Si-based photocathodes as the working electrode, Pt as the counter electrode, and Hg/HgO as the reference electrode. A potentiostat (CHI 660) was used to apply potential to the working electrode. The electrolyte was prepared by dissolving 1 M KOH in DI water. The photoelectrochemical performance was measured under chopped illumination from a 300 W Xe lamp equipped with AM 1.5 G. The calibration of the light intensity to 1 sun was conducted with a photometer. Before the measurements, nitrogen gas (≥99.999%) was injected into the electrolyte for at least 30 min to remove the dissolved oxygen. All the potential values can be calibrated against the reversible hydrogen electrode (RHE) using the following equation:

$$E_{RHE} = E_{Hg/HgO} + 0.097\ V + 0.059\ V \times pH \qquad (S1)$$

Linear sweep voltammetry was conducted at a scan rate of 10 mV s^{-1} and bias was applied from −0.2 to 0.6 V_{RHE}. For the stability test, the current density was measured using chronoamperometry at a bias of 0 V_{RHE} under continuous illumination.

Photoelectrochemical impedance spectroscopy (PEIS) was carried out at a potential from 0.2 to −0.2 V_{RHE} and the AC potential frequency ranged from 10^5 to 0.01 Hz under illumination.

Chronoamperometry measurements were carried out at a potential of 0 V_{RHE} in 1 M KOH under the simulated AM 1.5G illumination.

The gas products were analyzed by gas chromatography (GC-2060, Ruimin) equipped with a thermal conductivity detector (TCD) for quantifying H_2.

ABPE was calculated through the equation:

$$ABPE = \frac{j \times (0 - V)}{P_{in}} \times 100\% \quad (S2)$$

where *j* is the actual current density (mA/cm^2), V is the applied bias voltage (V_{RHE}), and P_{in} is the optical power density (mW/cm^2).

Two-electrode System

For the PEC tandem device for on **Ti/TiO$_2$/CdS/ZnSe** photoanode coupled with hydrogen production on **Si/PTH/CdS/CoP** photocathode, its photoelectrochemical tests were carried out in a square quartz electrolytic cell. A 0.25 M Na_2S+0.35 M Na_2SO_3 solution (pH 13.220) for anode electrolyte with a1.0 M KOH solution (pH 14) for cathode electrolyte was used for the bias-free PEC measurements.

STH in the two-electrode system was calculated through the equation:

$$\eta_{STH} = \frac{r_{H_2} \times \Delta G_{H_2}}{P_{in} \times A} \quad (S3)$$

r_{H_2} (Hydrogen production rate): mol/s

ΔG_{H_2}**:**(The heat of combustion of hydrogen)：285.8 kJ/mol.

P_{in} (Incident light power density)： 100 mW/cm^2 (AM 1.5G).

A (illumination area): cm^2

Butler-Volmer theory's plots

This equation describes the behavior of the photocurrent on the carrier density, diffusion length (L_p), applied potential (V), flat-band potential (V_B), the "width constant" of SCR (W_0), and wavelength of incident light (φ_0).

$$j = q\varphi_0\left(1 - \frac{\exp(-\alpha W_0(V - V_B)^{1/2}}{1 + \alpha L_p}\right) \qquad \text{(S4)}$$

A much simpler method for obtaining flat-band potentials is possible for $\alpha L_p <<< 1$. We can expand the above exponential for $\alpha W_o(V-V_B)^{1/2} <<< 1$. Then, the relation between applied potential and photocurrent density becomes

$$(V-V_B) \propto (J/\alpha W_0 q\varphi_0)^2 \qquad \text{(S5)}$$

in which α is the optical absorption coefficient, W_0 is the depletion width, and φ_0 is the light intensity.

The Gartner-Butler model assumes an ideal behavior, where V_0 is the flat-band potential, but the real onset potential for water reduction is more negative than the flat-band potential.

Supplementary Note S4:

The Charge Separation and Injection Efficiency

In principle, the photocurrent of HER ($J_{photocurrent}$) is a product of the rate of photon absorption expressed as a current density ($J_{absorbed}$), the charge separation yield of the photogenerated carriers ($P_{charge\ separation}$), and charge injection yield to the electrolyte ($P_{charge\ injection}$):

$$J_{photocurrent} = J_{absorbed} * P_{charge\ separation} * P_{charge\ injection} \quad (S6)$$

The photocurrent measured in the electrolyte with $K_3[Fe(CN)_6]$ ($J^{K3[Fe(CN)6]}_{photocurrent}$) is only a product of $J_{absorbed}$ and $P_{charge\ separation}$, assuming the charge injection yield becomes 100% ($P_{charge\ injection} = 1$) in the presence of a electron scavenger $K_3[Fe(CN)_6]$ in the electrolyte:

$$J^{K3[Fe(CN)6]}_{photocurrent} = J_{absorbed} * P_{charge\ separation} \quad (S7)$$

Based on the above equations, the charge injection yield can be achieved:

$$P_{charge\ injection} = J_{photocurrent} / J^{K3[Fe(CN)6]}_{photocurrent} \quad (S8)$$

The charge separation yield is given by:

$$P_{charge\ separation} = J^{K3[Fe(CN)6]}_{photocurrent} / J_{absorbed} \quad (S9)$$

Supplementary Note S5: DOS Equation

the space charge capacitance (C_{SC}), to (D), the DOS variable, as a surface potential is applied (ϕ_s) to modulate the Fermi level (E_F) of the electrode. This relationship includes the permittivity of free space (ε_0), the permittivity of the material (ε), and the charge of an electron (e).

$$D(E_f + \phi_s) = \frac{1}{\varepsilon\varepsilon_0 e} C_{sc}(\phi_s)^2 \quad \text{(S10)}$$

Variable	Value	Units
ε	11.8	Unitless
ε_0	8.854×10^{-14}	$\frac{C\ cm}{cm^2}$
e	1.602×10^{-19}	C
$C_{sc}(\phi_s)$	*Measured**	$\frac{C}{cm^2}$
$D(E_F+\phi_s)$	Calculated	$V^{-1}cm^{-3}$

*Note: The capacitance measured needs to be corrected manually for the experimental cell area before using it in the calculation of DOS so the units become F/cm^2. For our experiment, this value is 0.36 cm^2.

The space charge capacitance (C_{SC}) was collected in contact with 0.1 M $TBAPF_6$ in MeCN with an Ag/Ag^+ reference and platinum mesh counter electrode. Then, the

capacitance data was converted to DOS units according to eq S10.

Supplementary Note S5:

The Mott-Schottky measurements performed in MeCN contained 0.1 M $TBAPF_6$ with a sinusoidal modulation of 10 mV at a frequency of 400 Hz. The reference electrode and counter electrode is Pt wire and Pt sheet, respectively.

The reverse-bias dependence of the area-normalized differential capacitance in the depletion region of the semiconductor is given by the Mott-Schottky relation:

$$\frac{1}{C^2} = \frac{2}{A^2 \varepsilon_0 \varepsilon_r q N_A}\left(V_{app} - V_{fb} - \frac{k_B T}{q}\right) \quad \text{(S11)}$$

where A is the device area, ε_0 is the vacuum permittivity (8.85×10^{-14} F cm^{-1}), ε_r is the relative permittivity (11.68 F cm^{-1}), q is the unsigned charge on an electron (1.6×10^{-19} C), N_A is the accepter impurity concentration in the semiconductor, V_{app} is the difference between the applied potential and the redox potential of the solution, V_{fb} is the flat-band potential, K is Boltzmann's constant, and T is the temperature 298 K.

Supplementary Note S6:

OCP-derived carrier lifetimes

The decay curves of the open circuit potential (OCP) of the *p*-Si photoanodes with different layered structures provide not only information about the built-in electrical field but also the lifetime of the photogenerated charge carriers.

The carrier lifetime was quantified by：

$$\tau_n = -\frac{k_B T}{e}\left(\frac{dOCP}{dt}\right)^{-1} \qquad \text{(S12)}$$

where τ_n, k_B, T, e, and dOCP/dt are the carrier lifetime, Boltzmann's constant, temperature (K), charge of single electron and derivative of the OCP transient decay, respectively.

Under steady-state illumination, a larger band bending (as achieved in the Si/PTH/CdS/Co-P photocathode) provides a stronger driving force for charge separation, effectively suppressing recombination and allowing more carriers to reach the surface for HER. This is why the device exhibits superior PEC performance.

When the light is turned off, the system returns from the illuminated quasi-equilibrium (with flattened bands) to the dark equilibrium (with fully bent bands). In a device with larger band bending, the depletion region contains more stored spatial charge. The recombination of this stored charge upon light cessation is therefore more rapid, resulting in a shorter OCP decay time (25 μs for Si/PTH/CdS/Co-P, compared to 3 ms and 4 s for the control samples).

Supplementary Note S7:

Normalized parameter

A normalized parameter (D) is involved by the transient photocurrent result:

$$D = \frac{I_t - I_{st}}{I_{in} - I_{st}} \qquad \text{(S13)}$$

where I_t, I_{st}, and I_{in} are the time-dependent, steady-state and initial photocurrents, respectively.

Supplementary Note S8:

Raman spectroscopy was performed on the **Si/PTH/CdS/Co-P** photocathode before and after the stability test (Fig. 5e). Before the reaction, the spectrum exhibits characteristic peaks of the Si substrate at 520 cm^{-1} (transverse optical mode, TO) and 581.2/671.1 cm^{-1} (longitudinal acoustic mode, LA) (Physica B: Condensed Matter, 2023, 669, 415302), along with a strong second-order Raman band at ~970 cm^{-1} (Physical Review B, 1973, 7, 3685). Additional peaks at 420 and 434 cm^{-1} are attributed to Co–P (Chemical science, 2018, 9, 5322-5333), while those at 91 and 301 cm^{-1} originate from CdS (Macromolecular Symposia. 2023, 407, 2100441).

After 10 hours of operation, the Co–P-related peaks shift to 472.7 and 519.7 cm^{-1}, indicating a structural rearrangement of the Co–P phase. Notably, the signals from the Si substrate and CdS are no longer detectable. This attenuation is consistent with the morphological evolution observed by SEM (**Fig. 5f-g**): the fresh nanoflower-like Co–P structure transforms into a more continuous hexagonal prism overlayer after the reaction, which effectively shields the substrate signals. The increased intensity of the Co–P Raman response may also reflect structural rearrangement or surface enhancement effects.

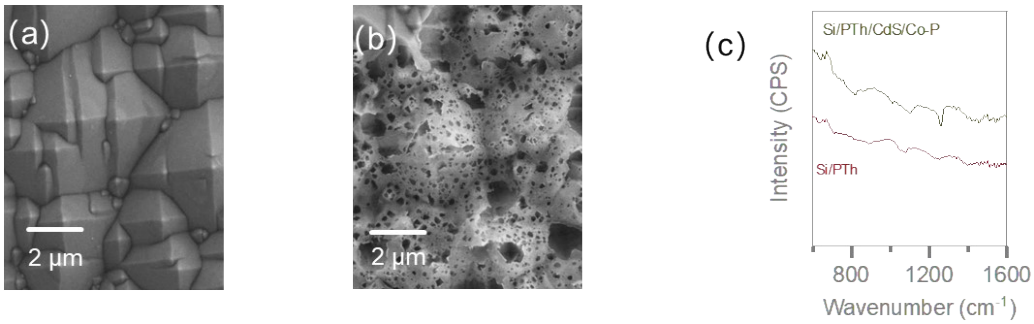

Supplementary Figure S1 ||SEM image on the surface of *p*-Si after wet chemical etching (a) and after (b) the PTH polymer. (c)

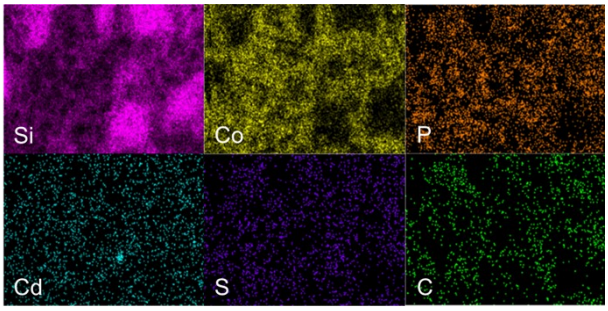

Supplementary Figure S2 || The EDS images for these elements for the **Si/PTH/CdS/Co-P** photocathode

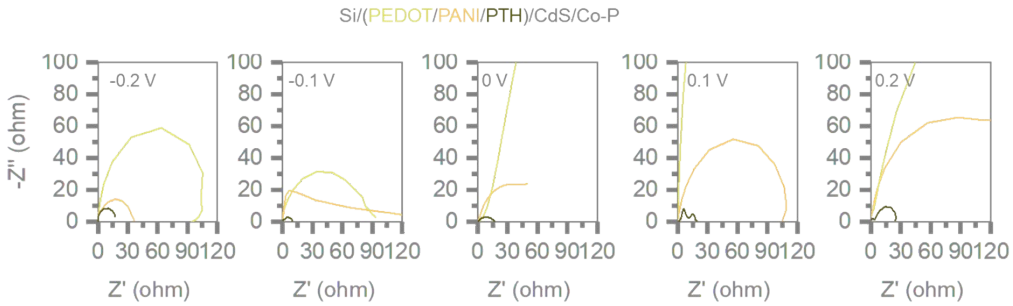

Supplementary Figure S3 | | Nyquist plots ranged from -0.2 to 0.2 V_{RHE}

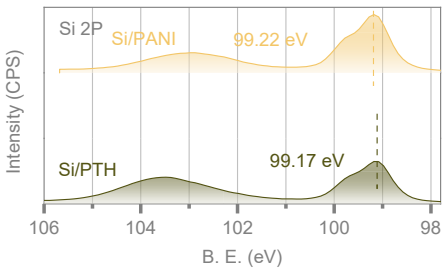

Supplementary Figure S4 ||High-resolution XPS for Si 2P on Si/PANI and Si/PTH electrode.

The Si 2p XPS spectra reveal that the Si⁰ peak, located at 99.4 eV for bare Si, shifts to lower binding energy by approximately 0.23 eV for Si/PTH and 0.18 eV for Si/PANI after polymer deposition. The interaction is therefore primarily electrostatic in nature, leading to the formation of an interfacial dipole layer.

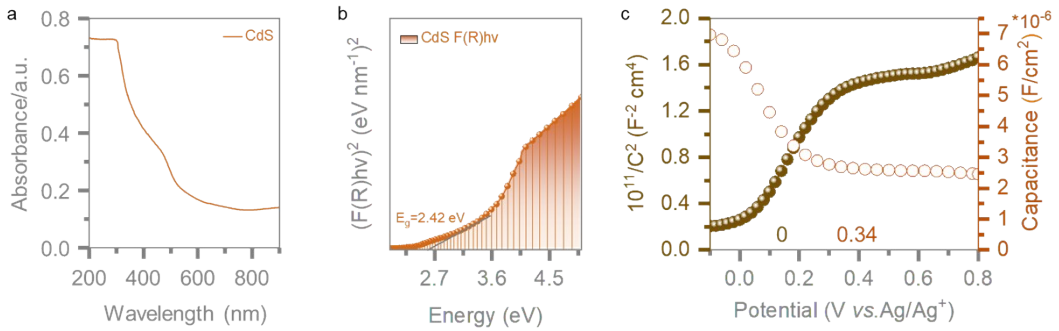

Supplementary Figure S5 | | Absorption spectrum (a), Tauc plot (b) and M-S plots (c) for CdS film

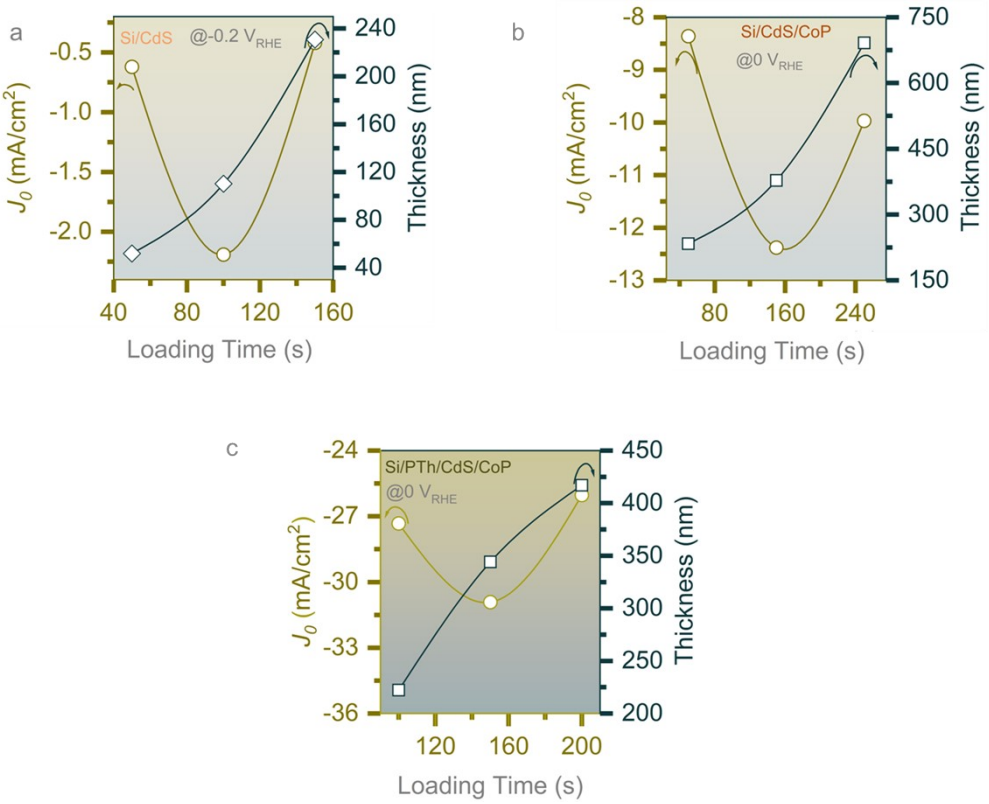

Supplementary Figure S6 || The thickness impact of CdS films (a), Co-P (b) and PTH films (c) on current density

As shown in **Figure S6**, the thickness of the as-prepared CdS, Co-P and PTH layer can be adjusted deposition time.

For the CdS layers, the photocurrent density at -0.2 V_{RHE} increases with the deposition time from 50 s to 100 s, and then decreases when deposition time extending to 150 s. Therefore, the CdS selects the 100 s deposition time of the optimal condition to subsequent preparation conditions (**Figure S6a**).

Compared their PEC performances on Co-P cocatalyst in **Figure S6b**. It is seen that the photocurrent density at 0 V_{RHE} increases with the deposition durations from 50 s to 150 s, and then decreases when the deposition time further extending to 250 s. Obviously, the

Co-P cocatalyst selected the deposition duration of 150 s presents the optimal PEC activity in the present work.

In **Figure. S6c**, the photocurrent density at 0 V_{RHE} increases with PTH deposition durations from 100 s to 150 s, and then decreases when deposition time extending to 200 s. Obviously, the 150 s deposition duration of PTH exhibits the optimal PEC activity in the present work.

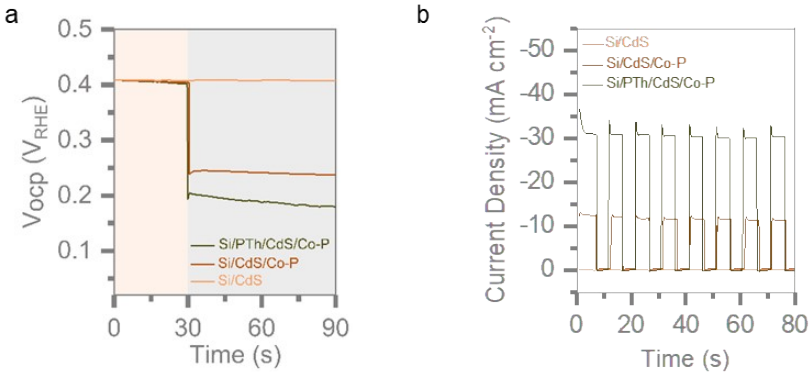

Supplementary Figure S7 | (a) Open-circuit potential transient decay. (b) The chopped current density over the three photocathodes at 0 V_{RHE} under one-sun condition.

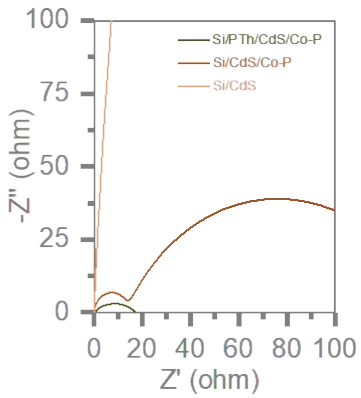

Supplementary Figure S8 || The Nyquist plots for the three photocathodes

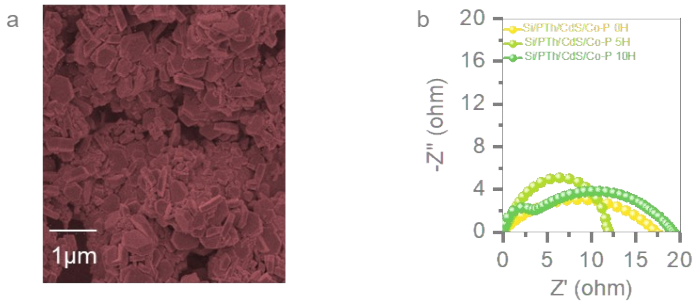

Supplementary Figure S9 | | (a) The SEM image for the **Si/PTH/CdS/Co-P** photocathode after 5 min of the stability test. (b) The Nyquist plots for the **Si/PTH/CdS/Co-P** photocathode after 0 h, 5 h, and 10 h of reaction.

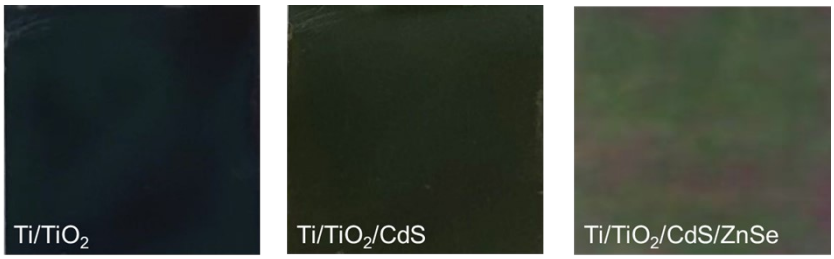

Supplementary Figure S10 ||The images for the photoanode

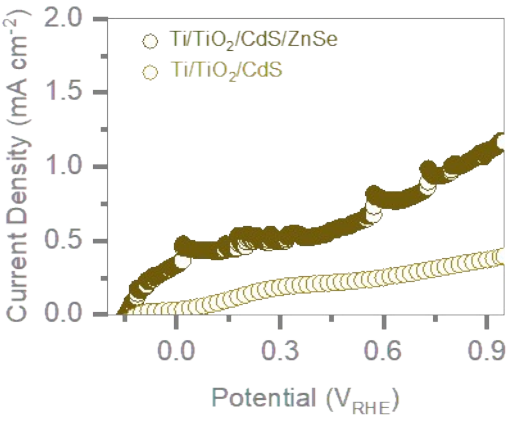

Supplementary Figure S11 | The PEC performance on these photoanodes in 0.25 M Na_2S+0.35 M Na_2SO_3 (pH=13.22) anolyte solution

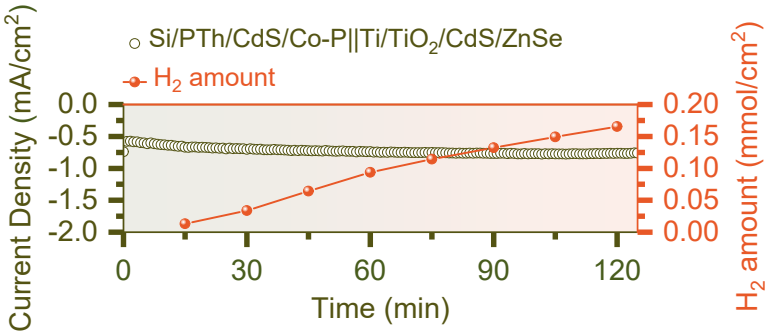

Supplementary Figure S12 | | The H_2 evolution for the two-electrode system

According to the eq S3, the STH of the two-electrode system was calculated to be 0.02%.

Supplementary Table S1 || The change in OCP between the dark and illuminated conditions

	Si/CdS	Si/CdS/Co-P	Si/PTh/CdS/Co-P
V_{ph} (mV)	1	172	220
OCP_{light}	427	422	414
OCP_{dark}	426	252	193

In the absence of illumination, the equilibrium between the photoelectrode and the electrolyte dictates that the measured open-circuit potential reports on the position of the Fermi level. Under illumination, the equilibrium between the electrolyte and the photoelectrode is maintained by the quasi-Fermi level of electrons; the Fermi level holes move in the positive direction. The difference between the newly measured potential (quasi-equilibrium) and that in dark (equilibrium) reports on the photovoltage.

Under illumination, the quasi-equilibrium potentials measured on these photocathodes should be comparable because this value is determined by the nature of the material. The key difference between the measured open-circuit potentials would be seen in the dark condition.

Supplementary Table 2. || The state-of-art performance over Si-based photocathodes in PEC-HER application.

Photocathodes	Onset Potential (V_{RHE})	Electrolyte	J_{sc} @ 0 V_{RHE}	Ref
p-Si/n-CdS	0.1	(Tri-HCl) buffer solution (pH = 6.8)	-1.45	**S1**
Si/CdS/TiO_2/Pt	0.42	1 M Phosphate buffer solution (pH 6.8)	-21.9	**S2**
p-Si/AZO/TiO_2/CoP_2	0.48	0.5 M H_2SO_4	-16.7	**S3**
Co-P/20WS_x/Si	0.47	1.0M KOH	-25.1	**S4**
Si/Co–NCNHP–TiO_2/CoP	0.18	0.5 M Na_2SO_4	-23.04	**S5**
Si/C_N/$TiO_{2(ALD/PP)}$/NiCoP	0.42	1.0M KOH	-19.87	**S4**
p-Si/PEIE/TiO_2/Pt	0.48	H_2SO_4 (pH 1)	-25.5	**S7**
Si@FeOOH/Ag/Cu_2O@Cu-CN	0.61	0.1 M KOH	-11.45	**S8**

Si/PANI/Cu_2O/SnS_x	0.45	1 M KOH	-21.64	**S9**
a-Si/Fh/Ni	0.57	1 M KOH	-15.6	**S10**
n+p-SiIP-T_4/TiO_2	0.11	0.1 M KOH	-2.4	**S11**
Si/MoS_2	0.16	0.5 M H_2SO_4	-0.16	**S12**
NNH/Si	0.28	0.5 M H_2SO_4	-18.9	**S13**
MoS_2/SnS_2/Si	0.23	0.5 M H_2SO_4	-23.8	**S14**
pn^+-Si/5nmTiO_2/WO_x-C	0.086	1 M KOH	-4.3	**S15**
SR $Ni_{0.95}Pt_{0.05}$Si	-0.05	0.5 M H_2SO_4	0	**S16**
p-Si/ WS_2/MoS_2	0.17	0.5 M H_2SO_4	-25	**S17**
MoS_2 NPs/TiO_2 NRs/p-Si	0.18	1 M KOH	-10	**S18**
This Work	0.31	1 M KOH	-30.08	

Reference

S1. Wu, S.; Li, L.; Qin, L.; Zhou, Z., Construction of p-Si/n-CdS Core/shell Nanowire Heterojunction for Photoelectrochemical Water Splitting. International Journal of Hydrogen Energy 2024, 73, 118-125.

S2. Liu, S.; Luo, Z.; Li, L.; Li, H.; Chen, M.; Wang, T.; Gong, J., Multifunctional TiO_2 Overlayer for *p*-Si/n-CdS Heterojunction Photocathode with Improved Efficiency and Stability. Nano Energy 2018, 53, 125-129.

S3. Li, H.; Wen, P.; Itanze, D. S.; Kim, M. W.; Adhikari, S.; Lu, C.; Jiang, L.; Qiu, Y.; Geyer, S. M., Retracted: Phosphorus-Rich Colloidal Cobalt Diphosphide (CoP_2) Nanocrystals for Electrochemical and Photoelectrochemical Hydrogen Evolution. Advanced Materials 2019, 31, 1900813.

S4. Li, S.; Lin, H.; Yang, G.; Ren, X.; Luo, S.; Wang, X.-s.; Chang, Z.; Ye, J., A Synergetic Strategy to Construct Anti-Reflective and Anti-Corrosive Co-P/WS_x/Si Photocathode for Durable Hydrogen Evolution in Alkaline Condition. Applied Catalysis B: Environmental 2022, 304, 120954.

S5. Li, X.; Zhao, H.; Huang, J.; Li, Y.; Miao, H.; Shi, G.; Wong, P. K., A High-performance TiO_2 Protective Layer Derived from Non-high Vacuum Technology for a Si-based Photocathode to Enhance Photoelectrochemical Water Splitting. Journal of Materials Chemistry A. 2024, 12, 16605-16616.

S6. Sun, X.; Liu, C.; Zhang, P.; Gong, L.; Wang, M., Interface-engineered Silicon Photocathodes with a NiCoP Catalyst-modified TiO_2 Nanorod Array Outlayer for Photoelectrochemical Hydrogen Production in Alkaline Solution. Journal of Power Sources

2021, 484, 229272.

S7. Yun, J.; Tan, J.; Jung, Y.-K.; Yang, W.; Lee, H.; Ma, S.; Park, Y. S.; Lee, C. U.; Niu, W.; Lee, J.; Kim, K.; Tilley, S. D.; Walsh, A.; Moon, J., Interfacial Dipole Layer Enables High-Performance Heterojunctions for Photoelectrochemical Water Splitting. ACS Energy Letters 2022, 7, 1392-1402.

S8. Jia, Y.; Cheng, Y.; Zhang, Y.; Ma, J., A p-n-p Configuration Based on the Cuprous Oxide/Silicon Tandem Photocathode for Accelerating Solar-Driven Hydrogen Evolution. ACS Applied Materials & Interfaces 2024, 16, 25551-25558.

S9. Ji, L.; Cheng, Y.; Qiang, Y.; Fu, X.; Jia, Y., Boosting the Performance of Cu_2O/p-Si Hybrid Photocathodes for Solar-Driven H_2 Generation: from Charge Dynamics to Thermodynamic Factors. ACS Applied Materials & Interfaces 2025, 17, 22519-22528.

S10. Zhang, D.; Du, M.; Wang, P.; Wang, H.; Shi, W.; Gao, Y.; Karuturi, S.; Catchpole, K.; Zhang, J.; Fan, F.; Shi, J.; Liu, S., Hole-Storage Enhanced a-Si Photocathodes for Efficient Hydrogen Production. Angewandte Chemie International Edition 2021, 60, 11966-11972.

S11. Lu, J.-H.; Li, Z.; Zhang, D.; Song, L.-H.; Cai, X.-Y.; Mao, L.; Liu, Z.-Q.; Wang, Z.-J.; Gu, X.-Q.; Yuan, G.-D., Enhanced solar hydrogen evolution by laminated integration of n+p-SiIP/TiO_2/Pt inverted pyramid black Si photocathode. Journal of Alloys and Compounds 2024, 1009, 176796.

S12. Yu, J.; Wang, Y.; Gai, Q.; Hou, C.; Luan, Z.; Liang, Y.; Liu, W.; Fan, X., Enhanced utilization of light through polystyrene microspheres for boosting photoelectrochemical hydrogen production in MoS_2/Si heterostructures. Journal of Materials Chemistry A 2025,

13, 8134-8143.

S13. Li, S.; Yang, G.; Ge, P.; Lin, H.; Wang, Q.; Ren, X.; Luo, S.; Philo, D.; Chang, K.; Ye, J., Engineering Heterogeneous NiS_2/NiS Cocatalysts with Progressive Electron Transfer from Planar *p*-Si Photocathodes for Solar Hydrogen Evolution. Small Methods 2021, 5, 2001018.

S14. Jena, A.; Pichaimuthu, K.; Leniec, G.; Kaczmarek, S. M.; Chang, H.; Su, C.; Hu, S.-F.; Liu, R.-S., Defect Mediated Improvements in the Photoelectrochemical Activity of MoS_2/SnS_2 Ultrathin Sheets on Si Photocathode for Hydrogen Evolution. ACS Applied Materials & Interfaces 2022, 14, 39896-39906.

S15. Liu, B.; Yang, J.; Li, F.; Liu, J.; Zhao, L.; Sun, L.; Chen, H.; Zhang, P.; Gao, L., WO_x-Carbon Nanorods Catalyzed Photoelectrochemical Hydrogen Evolution Reaction of Silicon-photocathode in Acidic Media. Chemical Engineering Journal 2024, 497. 154402.

S16. Zhang, H.; Li, S.; Xu, J.; Sun, X.; Xia, J.; She, G.; Yu, J.; Ru, C.; Luo, J.; Meng, X.; Mu, L.; Shi, W., Dissolution-Induced Surface Reconstruction of $Ni_{0.95}Pt_{0.05}Si$/p-Si Photocathode for Efficient Photoelectrochemical H_2 Production. Small 2024, 20, 2311738.

S17. Lee, J. Y.; Jun, S. E.; Shim, J. H.; Kang, H. S.; Kim, C.; Kim, K.; An, J. Y.; Choi, S.; Yun, J.; Kang, J.; Lee, S. W.; Park, S.; Lee, H.; Yi, Y.; Jang, H. W.; Lee, C. H., Wafer-Scale Semitransparent MoS_2/WS_2 Heterojunction Catalyst on a Silicon Photocathode for Efficient Hydrogen Evolution. Small 2024, 21, 2407650.

S18. Jun, S. E.; Hong, S. P.; Choi, S.; Kim, C.; Ji, S. G.; Park, I. J.; Lee, S. A.; Yang, J. W.; Lee, T. H.; Sohn, W.; Kim, J. Y.; Jang, H. W., Boosting Unassisted Alkaline Solar Water Splitting Using Silicon Photocathode with TiO_2 Nanorods Decorated by Edge-Rich MoS_2

Nanoplates. Small 2021, 17, 2103457.